CFD Analysis of Turbines and Compressors Used in Neon Turbo-Brayton Refrigerators

KAWAKUBO Tomoki : Deputy General Manager, Technology Platform Center, Technology & Intelligence Integration

YOSHINAGA Seiichirou : Manager, Electrification Development Group, Co-Creation Project Center, Technology & Intelligence Integration

ODA Kentarou : Doctor of Engineering, Manager, Electrification Development Group, Co-Creation Project Center, Technology & Intelligence Integration

KURIHARA Kazuaki : Manager, Electrification Development Group, Co-Creation Project Center, Technology & Intelligence Integration

KANEKO Yuudai : Doctor of Engineering, Development Department, Engineering Center, Vehicular Turbocharger Business Unit

Recently, High-Temperature Superconducting (HTS) appliances have been transitioning from the research phase to the product development stage. A turbo-Brayton refrigerator that uses neon gas as its working fluid is considered to be suitable for the cooling of large-scale equipment such as HTS cables. The reason for this is its compactness and high capacity, as well as its high reliability during long-term operation and relatively easy maintenance owing to its oil-free nature. IHI has been working with TAIYO NIPPON SANSO CORPORATION on the development of such a turbo-Brayton refrigerator since 2006. This report describes the CFD analysis that is used in the aerodynamic development of the turbines and compressors that constitute the refrigeration system.

1. Introduction

In recent years, devices using High-Temperature Superconducting (HTS) have been shifting from the research stage to that of practical use, with development advancing for their utilization as power-transmission lines, motors, generators, and transformers, etc. In addition, although Low-Temperature Superconducting (LTS) has been used in medical equipment such as Magnetic Resonance Imaging (MRI) and Nuclear Magnetic Resonance (NMR) devices, the utilization of HTS for these devices is now also being considered. These devices are cooled by regenerator-type refrigerators — such as Stirling, Gifford-McMahon (GM), and pulse tube refrigerators — which are accompanied by oscillating flow, or recuperator-type refrigerators — such as Joule-Thomson (JT) and Brayton refrigerators — which operates without oscillating flow. Amongst these, turbo-Brayton refrigerators are suitable for space-saving large-capacity applications, making them oil-free ensures long-term reliability, and their maintenance is relatively easy, therefore turbo-Brayton refrigerators may be considered suitable as the cooling system for large devices, such as HTS power transmission lines[1]-[5].

In cooperation with TAIYO NIPPON SANSO CORPORATION (TNSC), we have, since 2006, been engaged in the development of turbo-Brayton refrigerators using neon as the refrigerant. This report gives details of the Computational Fluid Dynamics (CFD) analysis used in the aerodynamic design of the turbine and compressor. In particular, we focus on the various special issues and points specific to the neon turbo-Brayton refrigerator, which differ from those involved in the design of turbines and compressors used in ordinary turbochargers and turbo-compressors.

2. Examples of research and development

A cooling system of an HTS power transmission line using a neon turbo-Brayton refrigerator consists of a liquid nitrogen loop for cooling the power transmission line and a neon loop for cooling the liquid nitrogen. **Figure 1** is a conceptual diagram of an HTS refrigeration system using a neon turbo-Brayton refrigerator. The neon turbo-Brayton refrigerator consists of ① a turbine operating at a low temperature of
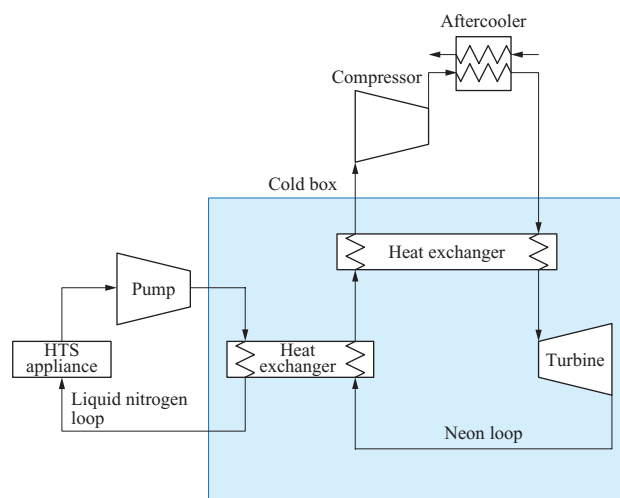

Fig. 1 HTS refrigeration system using a neon turbo-Brayton refrigerator

approximately 70 K, ② compressor operating at normal temperature, ③ aftercooler to release the heat of compression generated by the compressor, ④ heat exchanger to cool the neon to the turbine inlet temperature, and ⑤ heat exchanger to cool the liquid nitrogen, etc. The power generated by the turbine can be discarded in the brakes and resistors, or used to assist the motor that drives the compressor. **Figure 2** shows the state diagrams of the neon turbo-Brayton refrigerator (**(a) *ph* diagram**, **(b) *Ts* diagram**). The neon turbine or the neon turbine compressor is the key hardware of this refrigerator, and consist of ① a turbine impeller, ② compressor impeller, ③ high-speed rotor, ④ magnetic bearings supporting the high-speed rotor, ⑤ stationary gas passages (scroll, nozzle, diffuser) surrounding them, ⑥ heat shield structures, and ⑦ shaft seal structures, etc.

A number of studies on neon-refrigerant turbo-Brayton refrigerators for cooling HTS power transmission lines have been reported in recent years. In FY2006 and FY2007, in a study "Fundamental Superconducting Application Technologies (Phase II)" by New Energy and Industrial Technology Development Organization (NEDO), TNSC developed a 2-kW neon refrigerator consisting of a reciprocating compressor, variable nozzle turbine, and gas bearings[6]. Following this study, from FY2008 to FY2012, TNSC developed a 2-kW refrigeration system in NEDO study "Technological Development of Yttrium-Based Superconducting Power Equipment." The turbine and compressor of this system are mounted on separate rotors and supported independently with each own magnetic bearings. The turbine is a single-stage radial turbine with a nozzle, of pressure ratio 2, and is very small, with an impeller tip diameter of 32 mm and inlet blade height of 2.2 to 2.5 mm. Its maximum turbine efficiency is 0.7 to 0.72. The compressor is a two-stage centrifugal compressor in which a motor and magnetic bearings are installed between two impellers whose backs are facing each other. The compressor also exhibited an efficiency of approximately 0.7. This 2-kW system was subsequently commercialized as NeoKelvin®-Turbo in 2013[7]-[9].

The practical use of an HTS power transmission cable is considered to require a single-unit refrigeration capacity of 5 to 20 kW, and TNSC subsequently developed a 10-kW Brayton cycle system. This system also uses a two-stage centrifugal compressor, but each stage is supported separately with magnetic bearings, and driven by a motor and radial turbine. This 10-kW system was also commercialized in 2016[10],[11].

In NEDO study "High-Temperature Superconducting (HTS) Cable Demonstration Project," performed from FY2007 to FY2013, Mayekawa Mfg. Co., Ltd. developed a neon refrigeration system with a refrigeration capacity of 5 kW. This is also a two-shaft system using magnetic bearings; however, it utilizes a three-stage centrifugal compressor and single-stage radial turbine. In this system, the first- and second-stage compressor impellers are connected, with their backs facing each other, to the ends of a single shaft, and are driven by a motor. The third-stage compressor impeller and a turbine impeller are connected, with their backs facing each other, to the other shaft, and the compressor is driven by a motor and turbine[12],[13].

With regard to activity overseas, Air Liquide of France has developed various types of LTS cooling systems. In an HTS power transmission line project of Long Island Power Authority (LIPA) of the United States, a helium-refrigerant Brayton refrigerator using two screw compressors and a two-stage turbine was developed in LIPA-I. Following this, in LIPA-II, a helium-neon-mixed-refrigerant Brayton refrigerator using a three-stage centrifugal compressor and single-stage turbine was designed[14]-[16]. On the other hand, Korea Electric Power Corporation (KEPCO) of the Republic of Korea, in collaboration with Hongik University and Changwon National University, performed investigations for turbo-Brayton refrigerator systems for 2- or 10-kW application, and conducted aerodynamic designs of single-stage radial turbines for these systems[17]-[19].

All the above are examples of research and development of neon-refrigerant turbo-Brayton refrigerators for the cooling of HTS power transmission lines. In addition to these cases, research and development of small neon turbo refrigerators for space equipment is being performed in Europe and the United States, mainly by Creare in the United States. In these refrigerators, gas bearings are used, and the turbine speed is as high as several hundreds of thousands of rpm[20]-[23]. Creare is also engaged in research and development of neon
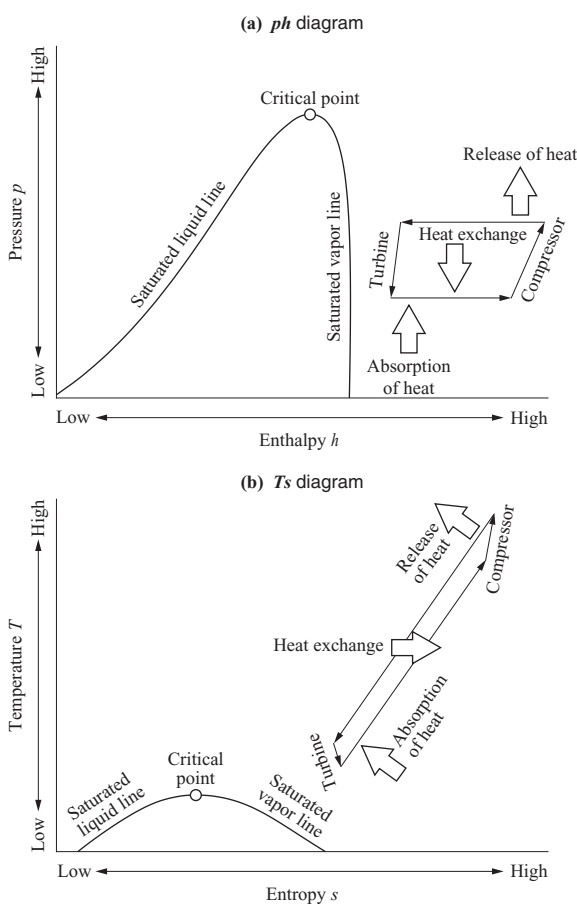

(a) *ph* diagram

(b) *Ts* diagram

Fig. 2   State diagrams for neon turbo-Brayton refrigerators

turbo-refrigerators for the air separation system in the C-17 transport aircraft[24].

3. CFD analysis of turbine for 2-kW research pilot unit

3.1 Specifications and characteristics of turbine

The turbine is a neon turbine designed for the 2-kW research pilot unit (hereinafter referred to as the 2-kW unit). **Table 1** lists the turbine's aerodynamic design specifications, and **Fig. 3** illustrates its shape. A major characteristic of the turbine is its narrow flow channel compared to the tip diameter of the impeller, which is due to the flow rate of the

Table 1 Aerodynamic design specifications for the turbine (2-kW research refrigerator)

Item	Unit	Value
Type		Radial
Inlet temperature	K	68
Inlet pressure	kPa	2 000
Outlet pressure	kPa	1 000
Rotor speed	rpm	98 000
Mass flow rate	kg/s	0.300

(a) Overall view of turbine

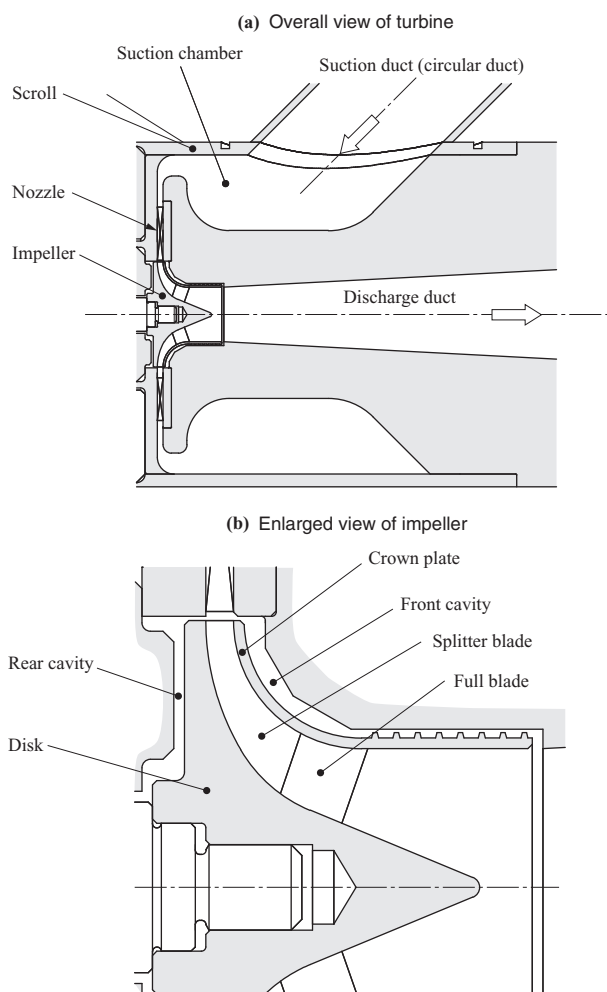**(b) Enlarged view of impeller**

Fig. 3 Configuration of the turbine for a 2-kW research refrigerator

refrigerant being small. Consequently, it is expected that use of an ordinary open impeller would result in a large decrease in efficiency due to the loss caused by clearance leakage. To reduce this loss, the turbine uses a closed impeller. In addition, although a large imbalance due to axial thrust is caused by no impeller being attached to the end of the shaft opposite to the turbine, the use of a closed impeller reduces this imbalance.

Furthermore, ordinary turbine impellers consist of blades that are all the same shape. In this turbine, however, a splittered impeller, in which short and long blades alternate, is used to achieve high performance. In addition, since the flow channel is narrow, it is afraid that design prediction errors and machining and assembly errors may have a significant effect, causing a mismatch between the nozzle and impeller. Therefore, in order to ensure that matching is adjustable during operation, a variable nozzle type is used whose nozzle vane has a changeable installation angle.

In the turbine design process, the velocity triangles were first roughly determined in accordance with the design specifications using one-dimensional analysis, and the detailed shapes of the blade, disk, and crown plate were then determined by CFD analysis and FEM (Finite Element Method) analysis.

3.2 CFD analysis method

ANSYS Fluent was used as the CFD solver. The solver was set as a density-based coupled solver, and the convection terms were descretized with a second-order accurate upwind scheme. As a turbulence model, the realizable k-ε model was used in conjunction with a wall function. The equivalent sand roughness corresponding to the value specified in the drawing was provided as the surface roughness of the passage.

To conduct the simulations efficiently, the turbine was divided into two sections, i.e., the scroll section (low-speed section), and nozzle and impeller section (high-speed section). From considerations of symmetry, a half model was used for the scroll section, with symmetric boundary conditions applied to the plane of symmetry. A full-annulus model was used for the nozzle section in order to take into account the influence of the non-axisymmetric flow from the scroll. The nozzle inflow conditions were extracted from the results of scroll analysis (the conditions obtained from reflection symmetry with respect to the symmetric boundary surface were applied). The nozzle was a variable nozzle, but was firmly fixed by plates at both ends, and the vane changed its angle rubbing on these plates, so that the clearances at both ends of the vane were assumed to be zero. The impeller section was represented by a periodical symmetry model for one pitch (the non-axisymmetry from the scroll was assumed to be absorbed by the nozzle and absent at the impeller inlet). In addition, the front and rear cavities were also modeled. A mixing plane is used as the interface between the rotor and stator. **Figure 4** illustrates the meshes used in CFD analysis.

3.3 Real gas effect

Since neon molecules are monatomic, no intermolecular

(a) Scroll

(b) Nozzle

(c) Impeller (meridional view)
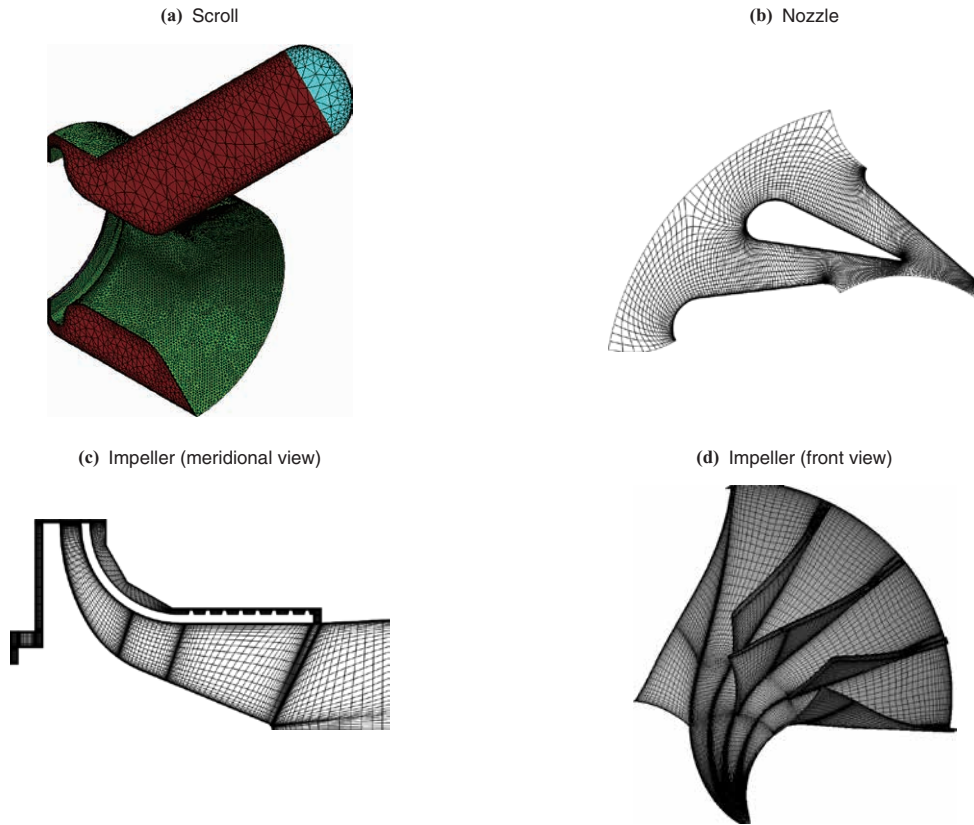
(d) Impeller (front view)

Fig. 4   CFD analysis mesh

forces act on them, and the real gas effect is not very strong around normal temperatures. However, as shown in **Table 1**, the turbine operates in a cold state, and the value of the compressibility factor is slightly smaller than 1, ranging from 0.96 to 0.97. This means that, although the real gas effect is not qualitatively conspicuous, it cannot be quantitatively ignored.

REFPROP and GASPAK, etc., are available as gas property databases, and GASPAK is used in this report. The Redlich-Kwong, Peng-Robinson, and virial models, etc., are equation-of-state models that can represent real gas effects, and all exhibit sufficient predictive accuracy for the aerodynamic design of turbines and compressors[25]-[27]. In this analysis, the Aungier-Redlich-Kwong equation-of-state model[28] was used. For nonequilibrium properties (viscosity and thermal conductivity), approximate polynomials, second-order in density and first-order in temperature, were formulated and used. The source data for approximations was calculated using GASPAK.

However, CFD analysis using the above-mentioned real gas model calculation results in a large calculation load, and requires complicated post-processing. Therefore, in the aerodynamic design, an approximate perfect gas model was also used. The properties for the perfect gas model (gas constant R, ratio of specific heat γ, isochoric specific heat C_v, and isobaric specific heat C_p) are set in accordance with the following equations (1) to (4)[25]-[27].

$$R = \frac{p_{01}}{\rho_{01} T_{01}} \quad \text{...(1)}$$

$$\gamma = \frac{\rho_{01} c_{01}{}^2}{p_{01}} \quad \text{...(2)}$$

$$C_v = \frac{1}{\gamma - 1} R \quad \text{...(3)}$$

$$C_p = \frac{\gamma}{\gamma - 1} R \quad \text{...(4)}$$

Here, p_{01}, T_{01}, ρ_{01}, and c_{01} refer respectively to pressure, temperature, density, and speed of sound at the turbine inlet under stagnation condition. By applying these settings, the performance parameters used for or obtained from perfect gas analysis, such as turbine speed, mass flow rate, and adiabatic enthalpy drop, can be used conveniently without converting into the values for a real gas state. The viscosity μ and thermal conductivity λ of the perfect gas are approximated by Sutherland formulae.

$$\mu = \mu_0 \frac{T_0 + S}{T + S} \left(\frac{T}{T_0} \right)^{3/2} \quad \text{..............................(5)}$$

$$\lambda = \lambda_0 \frac{T_0 + S}{T + S} \left(\frac{T}{T_0} \right)^{3/2} \quad \text{..............................(6)}$$

$$\lambda_0 = \frac{C_p \mu_0}{Pr} \quad \text{...(7)}$$

Here, T_0 represents an arbitrary reference temperature. Using

GASPAK, the viscosity μ in a low pressure state is expressed as $\mu(T)$, a function of temperature T, and $T^{3/2}/\mu(T)$, a function of temperature expressed using $\mu(T)$, is then approximated to the form $aT + b$ within the anticipated temperature range by the least square method. Using the a and b values obtained in this process, the constant S and reference viscosity μ_0 can be expressed by the following equations.

$$S = \frac{b}{a} \quad \text{...(8)}$$

$$\mu_0 = \frac{T_0^{3/2}}{aT_0 + b} \quad \text{...(9)}$$

In the same manner, the Prandtl number Pr can be determined within the anticipated temperature range as the average value of $C_p\mu(T)/\lambda(T)$, a function of temperature obtained using GASPAK.

Figure 5 shows comparisons between turbine performance prediction by the real gas and perfect gas models. Although a slight difference of approximately 0.2 points is exhibited in adiabatic efficiency, no significant differences are observed that might affect decisions on aerodynamic design. This shows that the perfect gas model has sufficient practical accuracy to simulate the real gas effect.

3.4 Results of CFD analysis

Figure 6 illustrates the flow pattern inside the scroll. **Figure 6-(a)** shows streamlines, in which the long line segments correspond to high flow speeds, and short line segments to low flow speeds. **Figure 6-(b)** shows the distribution of loss coefficient value in the sections shown in the streamline diagrams in **-(a)**; the flow from the suction duct enters the scroll like as a jet, where it blows directly into the nozzle passage. Apart from this jet-like blowing flow, there is another that forms a slow recirculation in the suction chamber. Around the blowing flow, there are high-loss regions due to the separation associated with rapid expansion of the passage. This separation is caused by rapid expansion of the passage area from the suction duct to the suction chamber, and by the axisymmetric annulus shape of the suction chamber.

Figure 7 illustrates the circumferential distribution of flow angle at the nozzle inlet. Ideally, it is desirable that the flow angle at the nozzle inlet be zero in all circumferential positions. However, around the position at azimuthal angle 0 degrees, there is a swirling flow of approximately 12 degrees. There is no appreciable flow distortion in the span direction.

Overall, no distortion that might cause concern at the nozzle inlet occurs inside the scroll, and the ratio of the loss caused by the scroll to the overall performance of the turbine is small, and therefore not at a level that would result in any problems.
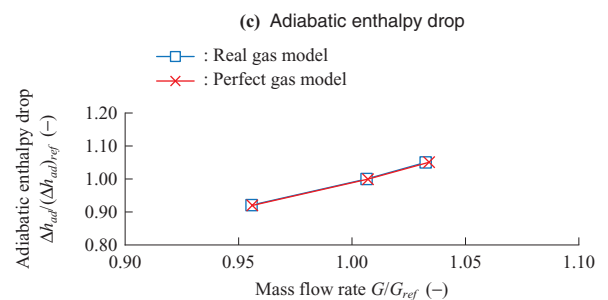
Figure 8 shows the overall performance of the turbine (pressure ratio π, adiabatic efficiency η_{ad}), the performance of the impeller alone (pressure ratio π_{imp}, adiabatic efficiency η_{ad_imp}), and nozzle effectiveness η_{NZL}. The parameters are defined by the following equations, and in the figure, they are normalized with respect to the design specification values.


(a) Mach number at nozzle outlet

□ : Real gas model
✕ : Perfect gas model
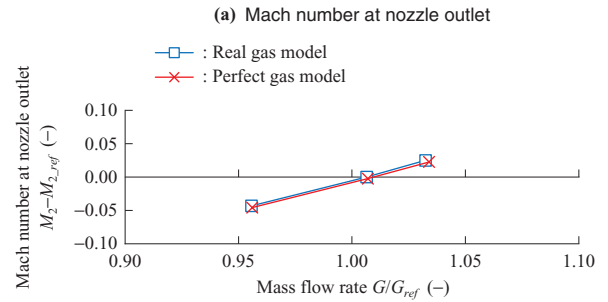
(Note)　G　　 : Mass flow rate
　　　　G_{ref}　 : Reference mass flow rate
　　　　M_2　　 : Mach number at nozzle outlet
　　　　M_{2_ref} : Reference Mach number at nozzle outlet

(b) Flow angle at nozzle outlet

□ : Real gas model
✕ : Perfect gas model
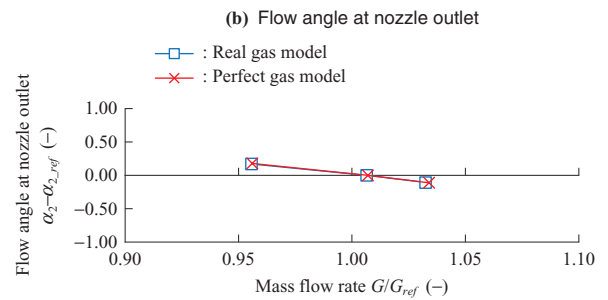
(Note)　α_2　　 : Flow angle at nozzle outlet
　　　　α_{2_ref} : Reference flow angle at nozzle outlet

(c) Adiabatic enthalpy drop

□ : Real gas model
✕ : Perfect gas model

(Note)　Δh_{ad}　　 : Adiabatic enthalpy drop
　　　　$(\Delta h_{ad})_{ref}$: Reference adiabatic enthalpy drop

(d) Adiabatic efficiency

□ : Real gas model
✕ : Perfect gas model
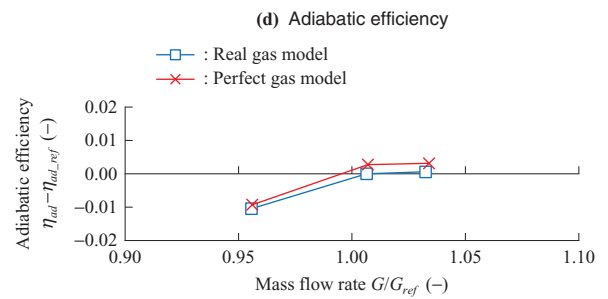
(Note)　η_{ad}　　 : Adiabatic efficiency
　　　　η_{ad_ref} : Reference adiabatic efficiency

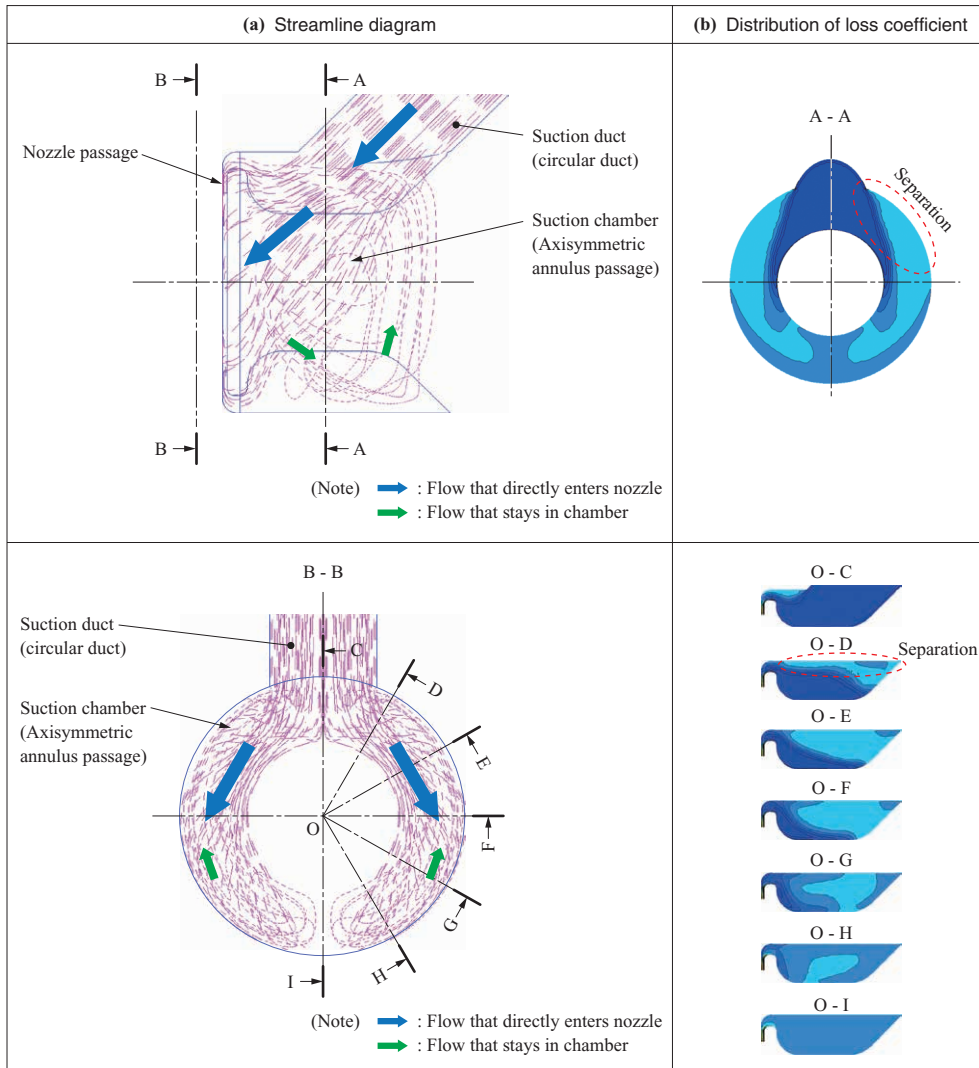**Fig. 5　Comparison of turbine performance predictions using a real gas model and a perfect gas model**
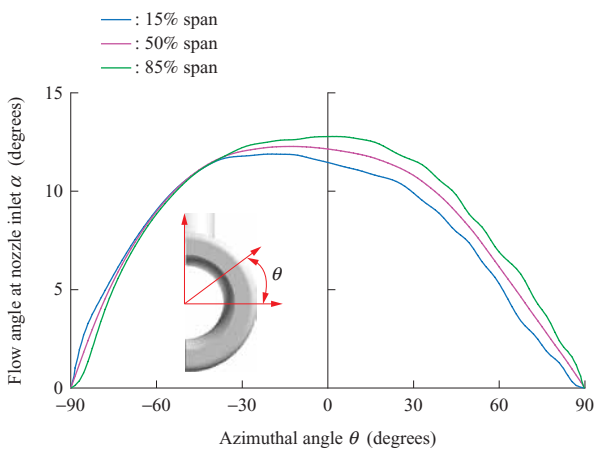
Fig. 6 Flow pattern inside the scroll

Fig. 7 Circumferential distribution of the flow angle at the nozzle inlet

$$\pi = \frac{p_{01}}{p_4} \quad \cdots\cdots\cdots\cdots\cdots\cdots\cdots\cdots\cdots\cdots(10)$$

$$\eta_{ad} = \frac{h(T_{01}, p_{01}) - h(T_{04}, p_{04})}{h(T_{01}, p_{01}) - h(s_1, p_4)} \quad \cdots\cdots\cdots\cdots(11)$$

$$\pi_{imp} = \frac{p_{03}}{p_4} \quad \cdots\cdots\cdots\cdots\cdots\cdots\cdots\cdots\cdots(12)$$

$$\eta_{ad\_imp} = \frac{h(T_{03}, p_{03}) - h(T_{04}, p_{04})}{h(T_{03}, p_{03}) - h(s_3, p_4)} \quad \cdots\cdots(13)$$

$$\eta_{NZL} = \frac{h(T_{01}, p_{01}) - h(T_3, p_3)}{h(T_{01}, p_{01}) - h(s_1, p_3)} \quad \cdots\cdots\cdots\cdots(14)$$

Here, suffix numbers 1, 3, and 4 indicate the turbine inlet, impeller inlet, and turbine outlet respectively, and suffix 0 indicates the stagnant conditions. T, p, h, and s respectively indicate temperature, pressure, enthalpy, and entropy. The adiabatic efficiency of the impeller includes the disk friction loss from the front face of the crown plate and rear face of the disk, and the leakage loss in the front cavity. At nozzle opening $\alpha_{NZL} = 0$ degrees and a design pressure ratio $\pi = 2$, the flow rate is almost in accordance with the specified flow rate, $G = 0.3$ kg/s. The difference between the overall efficiency of the turbine and the efficiency of the impeller
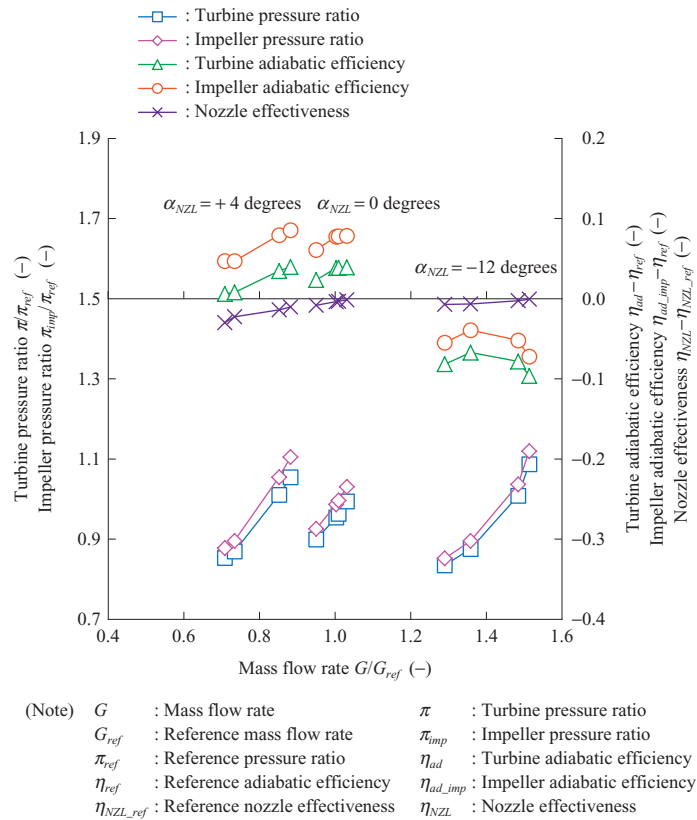
: Turbine pressure ratio
: Impeller pressure ratio
: Turbine adiabatic efficiency
: Impeller adiabatic efficiency
: Nozzle effectiveness

$\alpha_{NZL} = +4$ degrees $\quad \alpha_{NZL} = 0$ degrees

$\alpha_{NZL} = -12$ degrees

(Note)	G	: Mass flow rate	π	: Turbine pressure ratio
	G_{ref}	: Reference mass flow rate	π_{imp}	: Impeller pressure ratio
	π_{ref}	: Reference pressure ratio	η_{ad}	: Turbine adiabatic efficiency
	η_{ref}	: Reference adiabatic efficiency	η_{ad_imp}	: Impeller adiabatic efficiency
	η_{NZL_ref}	: Reference nozzle effectiveness	η_{NZL}	: Nozzle effectiveness

Fig. 8 Overall performance of the turbine, performance of the impeller alone, and nozzle effectiveness

alone is 3 to 4 points, so the performance of the impeller dominates overall performance.

Figure 9 shows the distribution of flow angle in the nozzle mean section. Due to the non-axisymmetry caused by the upstream scroll shape (see **Fig. 7**), a non-axisymmetric distribution is observed on the upstream side of the vane, whereas these variations disappear at the mid-chord and the rear part of the nozzle passage. No separation or reverse flow that might cause problems is observed at the nozzle inlet or between vanes, so, as a whole, the flow pattern is preferable.

Figure 10 shows the impeller disk friction losses and leakage loss. The efficiency loss due to disk friction is about 1 point. This value is not very large when compared to the efficiency decrease in the impeller (12 to 24 points). Disk friction loss occurs on both the front face of the crown plate and rear face of the disk. However, the loss on the front face of the crown plate, across which exists an inward flow, is smaller than that on the rear face of the disk, across which flow is (assumed to be) completely absent[29]. In contrast, the efficiency loss due to front cavity leakage is 4 to 5 points at around $\pi = 2$, one of the largest loss sources in the impeller.

Figure 11 shows the distribution of entropy on cross sections along the flow direction inside the impeller. Generation of entropy due to separation is observed near the inlet. The loss on the suction surface that occurs due to separation is transferred, together with loss of the suction surface boundary layer, to the shroud side by the secondary flow, where it accumulates at the corners formed by the shroud and suction surfaces to form high-loss regions. However,

(a) Flow angle contour ($\alpha_{NZL} = 0$ degrees)

Flow angle
(−)

High

Low
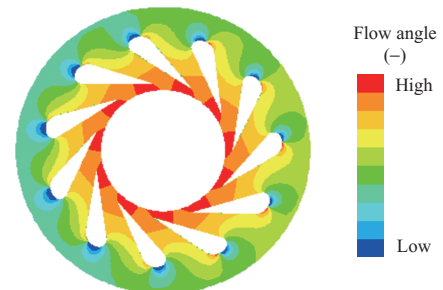
(b) Flow angle distribution ($\alpha_{NZL} = 0$ degrees)

: Upstream side of nozzle
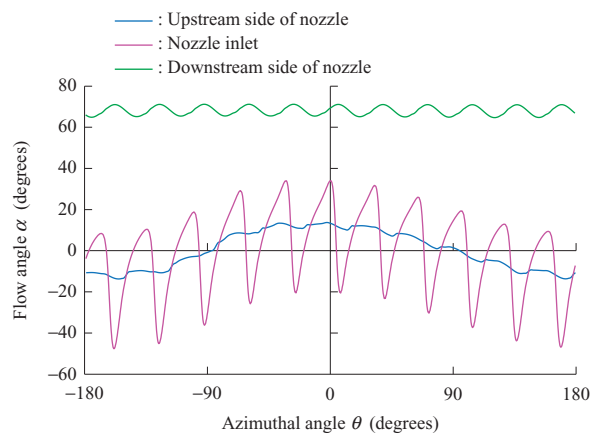: Nozzle inlet
: Downstream side of nozzle

Fig. 9 Distribution of the flow angle in the nozzle mean section
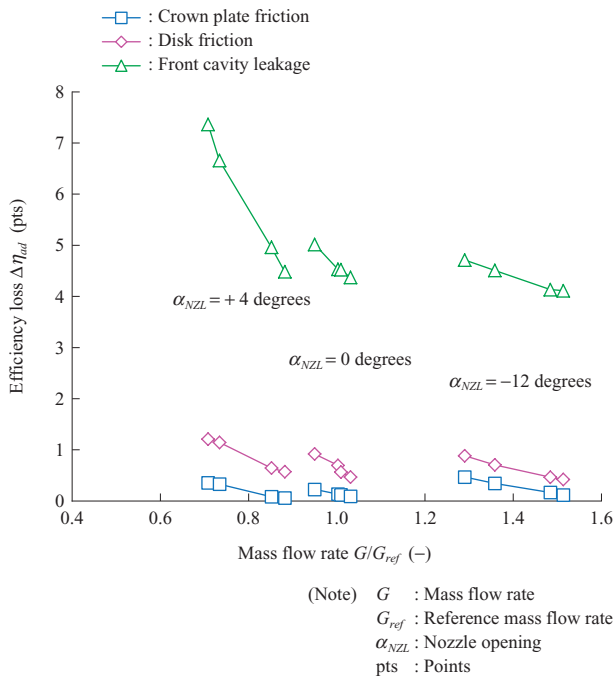
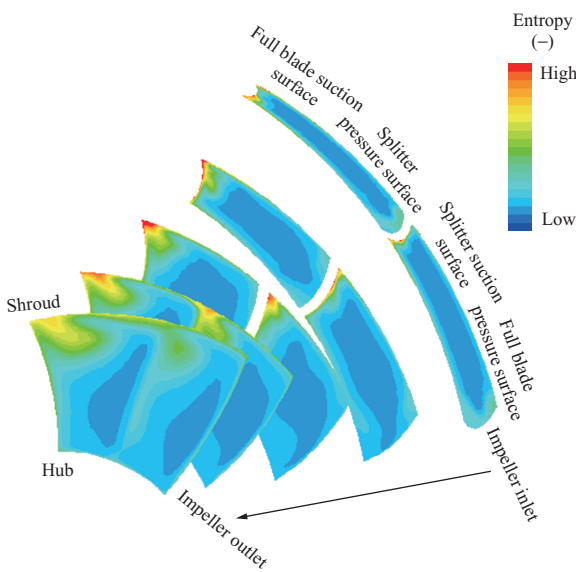**Fig. 10 Impeller disk friction loss and leakage loss**

Fig. 11 Distribution of entropy at cross-sectional planes along the flow direction inside the impeller

these high-loss regions result from accumulation of losses flowing from the upstream side, and since no accompanying corner separation occurs, these regions in themselves are not considered to constitute a cause of any further loss.

3.5 Summary of turbine for 2-kW unit

The design of this turbine has involved proactive, ambitious attempts, such as a closed impeller, splittered impeller, and variable nozzle, etc. There are no problematic losses — apart from that due to separation caused by the non-axisymmetry of the scroll and leakage loss in the front cavity — and the flow field is, overall, of a favorable nature. In addition, the influence of the loss in the scroll on the overall performance of the turbine is not very large. This turbine was incorporated

into a 2-kW unit and exhibited good performance in actual operation. Going forward, it is desirable to reduce leakage loss in the front cavity, and develop design and machining technologies that will take greater advantages of closed impellers over open impellers.

4. CFD analysis of turbine and compressor for 10-kW unit

4.1 Specifications and characteristics of turbine

Table 2 lists the aerodynamic design specifications of a turbine for a neon-turbine compressor used in 10-kW unit. For 10-kW unit, the impeller blade height is not as small as that for 2-kW unit. The inlet pressure is lower than that for 2-kW unit, and a compressor impeller is attached to the opposite end of the shaft. In addition, magnetic bearings are used for 10-kW unit, whereas foil bearings are used for 2-kW unit. In consideration of these differences in form, an open impeller — not a closed impeller — is used in this turbine. Furthermore, the impeller is of an ordinary type with no splitter blades, and a fixed-type turbine nozzle is employed.

Figure 12 illustrates a cross section of the turbine compressor for 10-kW unit, and **Fig. 13** shows impeller and nozzle shapes. This turbine is characterized by a large impeller inlet blade height which is 1.6 times the nozzle vane height (**Fig. 13-(b)**: Case 2). For the purposes of comparison, operation using an impeller with an inlet blade height equal to the nozzle vane height (**Fig. 13-(a)**: Case 1) was also investigated. Investigation was also performed on a configuration with a nozzle vane height equal to the impeller inlet blade height (**Fig. 13-(c)**: Case 3), but, since the nozzle exit condition deteriorated and the efficiency decreased substantially, no further description is given below on this configuration. Since the minimum blade thickness of the turbine impeller is quite small on the shroud side, cutting work is expected to be difficult. Therefore, as a backup type, comparison for an impeller with 1.5 times blade thickness was also performed. Similarly, for the nozzle, it may be necessary for structural reasons to make the vane leading edge blunt (by thickening the vane leading edge), and in order to check that this does not cause performance problems, operation using thick nozzle vanes was compared with that using thin vanes. **Figure 13-(d)** illustrates the thin and thick nozzle vane shapes. The two nozzles are designed to have substantially different shapes at the leading edge but almost the same at the trailing edge, and have almost equal throat width and throat position.

Table 2 Aerodynamic design specifications for the turbine (10-kW refrigerator)

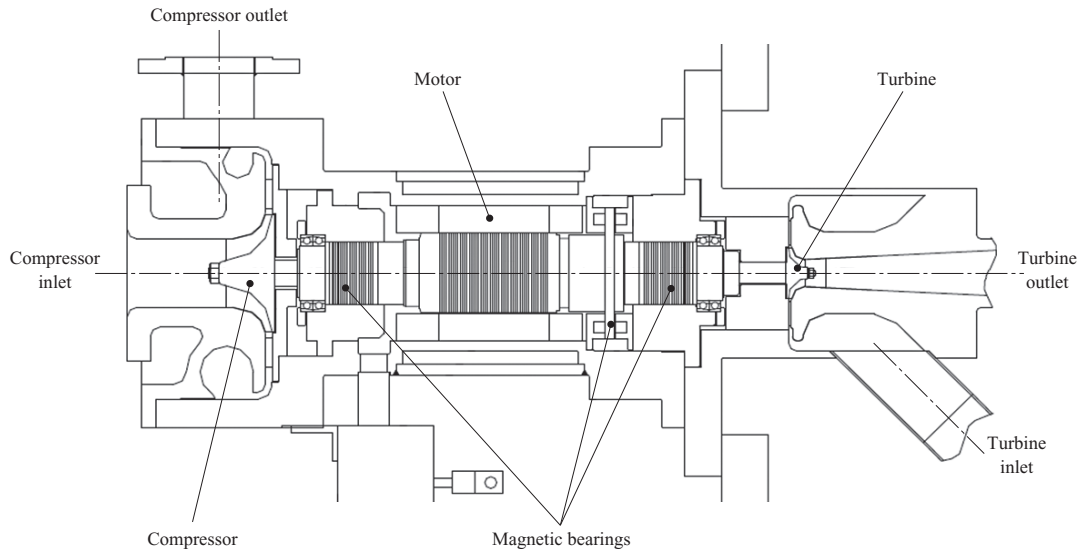| Item	Unit	Value
Type		Radial
Inlet temperature	K	73
Inlet pressure	kPa	987
Outlet pressure	kPa	540
Rotor speed	rpm	42 000
Mass flow rate	kg/s	0.480

Fig. 12 Cross-section of the turbine-compressor for a 10-kW refrigerator
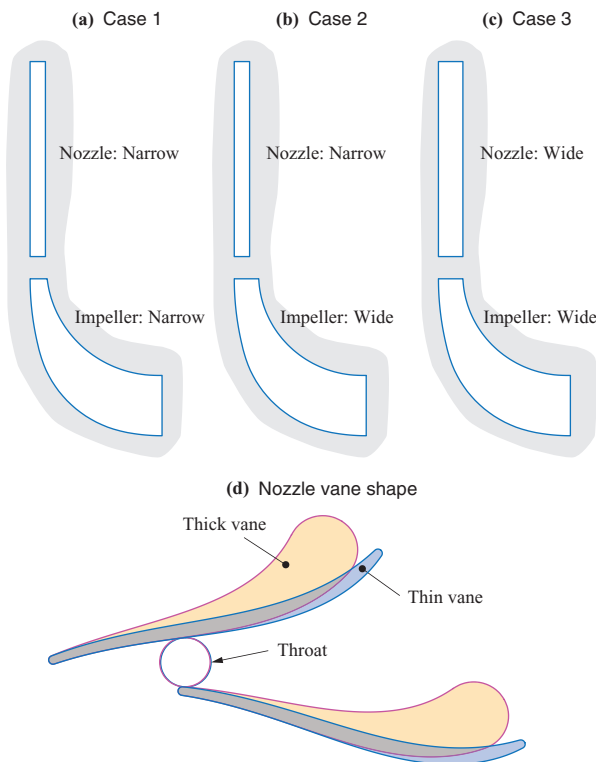

Fig. 13 Impeller shape and nozzle shape

4.2 Turbine CFD analysis method

As described in **Chapter 3**, the pressure loss of the scroll does not have a significant influence on the overall performance of the turbine, so, in the turbine CFD analysis in **Section 4.2**, the scroll was not modeled, but only the nozzle and impeller. The flow angle at the nozzle inlet was set to zero. However, as described in **Section 3.4**, depending on circumferential position, the flow angle at the nozzle inlet may differ within a range of approximately −10 to +10 degrees due to the non-axisymmetry of the scroll's shape. We therefore performed another CFD analysis in which the flow angle at the nozzle inlet was changed within this range,

thereby confirming that the difference in efficiency resulting from such changes was at the level of 0.1 points or less, and could therefore be ignored.

The analysis was performed by using the perfect gas model described in **Section 3.3**. A finite difference method solver for the compressible and viscous Navier-Stokes equation that was developed in-house to analyze the turbomachinery blade rows was used as the CFD solver. The Chakravarthy-Osher Total Variation Diminishing (TVD) scheme was applied to the convection terms, and the one-equation Spalart-Allmaras model was used as the turbulence model. The domain connection between rotor and stator was implemented using mixing planes.

4.3 Results of turbine CFD analysis

First, we discuss the influence of the apparent difference between nozzle vane height and impeller inlet blade height. **Figure 14** shows the results of prediction of overall turbine performance in Cases 1 and 2. In both cases, the specified flow rate is satisfied at the design pressure ratio, and, at that point, the efficiency in Case 2 is higher than that in Case 1 by approximately 0.7 points. To identify the cause of this difference, the internal flow in the nozzle and that in the impeller were analyzed in detail.

Figure 15 shows the spanwise distributions of entropy at the nozzle outlet and impeller inlet. On the hub side, almost no entropy increase between the nozzle outlet and the impeller inlet is observed in Case 2, whereas a slight entropy increase is observed in Case 1. This is presumed to be because, in Case 1, the smaller passage width makes the flow speed higher. In contrast, on the shroud side, the entropy increase is large in Case 2 which is considered to occur at the convex corner formed by the expansion of passage width.

In Case 2, the large expansion of flow channel width on the downstream side of the nozzle causes a concern on the possibility of the occurrence of reverse flow or separation on the shroud side. **Figure 16** shows the spanwise distributions of radial velocity at the nozzle outlet and impeller inlet. The
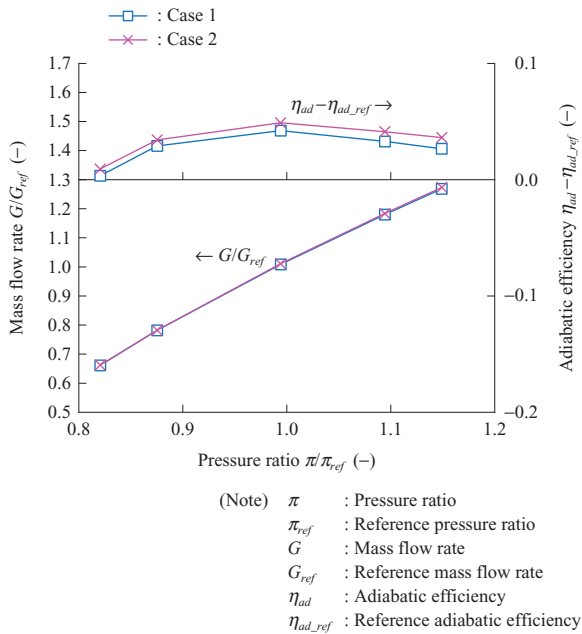
(Note)
π : Pressure ratio
π_{ref} : Reference pressure ratio
G : Mass flow rate
G_{ref} : Reference mass flow rate
η_{ad} : Adiabatic efficiency
η_{ad_ref} : Reference adiabatic efficiency

Fig. 14 Predicted overall turbine performance

(Note)
s : Entropy
R : Gas constant

Fig. 15 Spanwise distribution of entropy at the nozzle exit and the impeller inlet

(Note)
C_r : Radial velocity
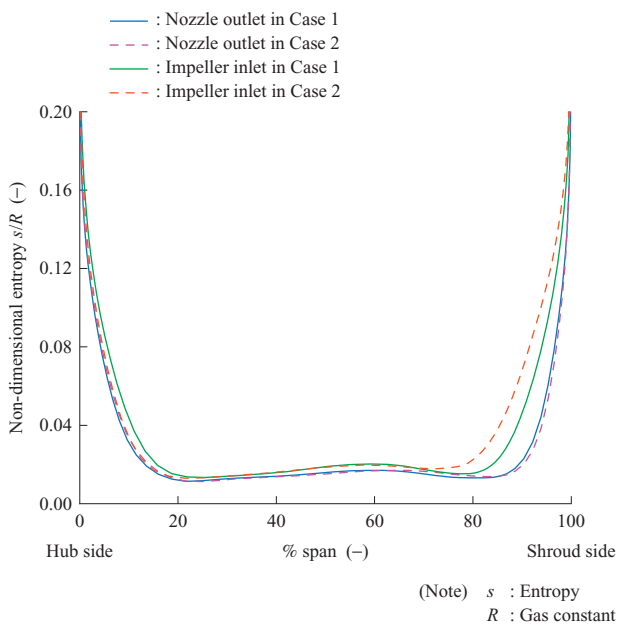U_3 : Impeller tip speed
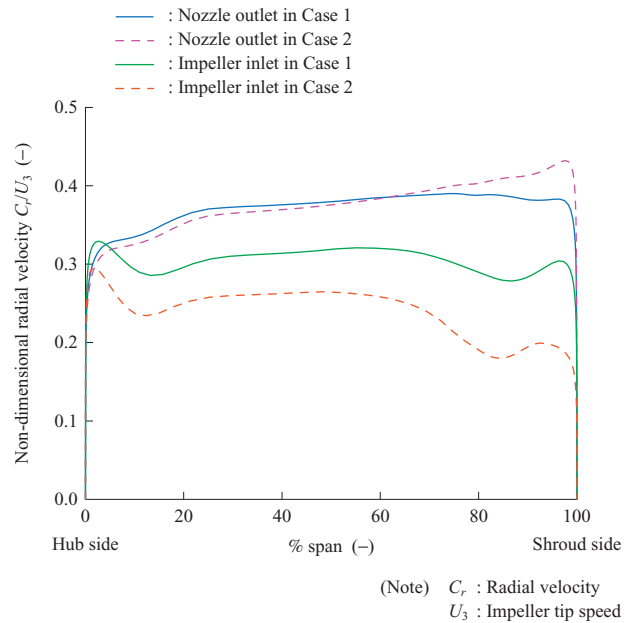
Fig. 16 Spanwise distribution of radial velocity at the nozzle exit and the impeller inlet

radial velocity decreases significantly more in Case 2 than Case 1, but no sign of separation of the boundary layer on the shroud side is observed. This is presumed to be because, for inward radial flow, the defect of radial velocity due to pressure loss inside the boundary layer is supplemented by the inward secondary flow developed by the inward secondary flow developed by the radial pressure gradient that is created by swirling flow (though a corresponding deficit of swirl velocity occurs).

Next, we discuss the difference in entropy increase inside the impeller. Increasing the impeller inlet blade height is expected to result in the following advantages.

(1) The widened passage width reduces the amount of blowing flow in the clearance.

(2) For the same turbine work, the widened blade area reduces blade loading per unit area (differential pressure), reducing clearance leakage.

(3) The increased passage height reduces radial velocity, and increases negative incidence on the shroud side, thereby suppressing the separation and clearance leakage that accompanies rapid load increase at the leading edge.

To confirm the effects of these advantages, **Fig. 17** shows the velocity distribution of clearance leakage flow, and **Fig. 18** shows the distribution of static pressure around the blade tip near the leading edge of the impeller. Blade loading (differential pressure) on the leading edge side is smaller in Case 2 than in Case 1, and leakage flow velocity is accordingly smaller, so that the influence of clearance leakage flow
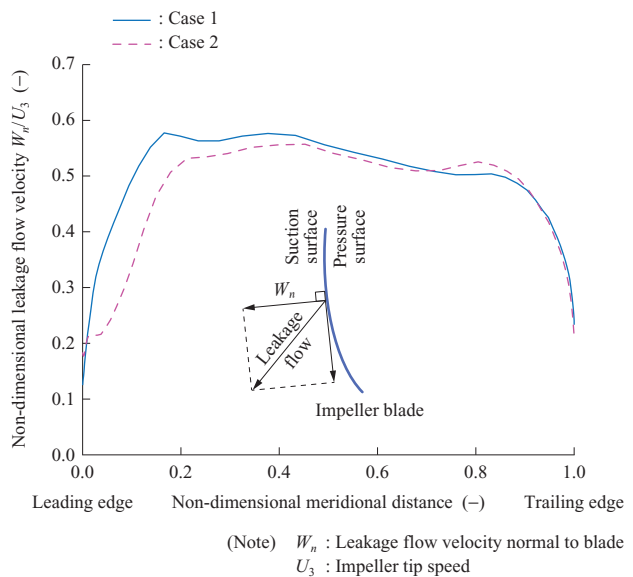

(Note)
W_n : Leakage flow velocity normal to blade
U_3 : Impeller tip speed

Fig. 17 Velocity distribution of the clearance leakage flow
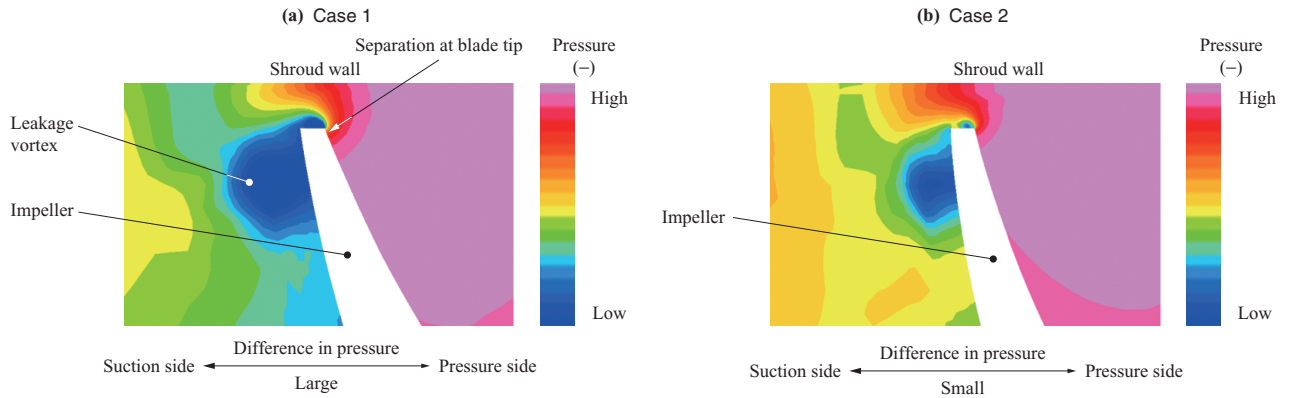
(a) Case 1

(b) Case 2

Fig. 18 Distribution of static pressure around the blade tip near the impeller leading edge

should be reduced.

The above discussion shows that, for turbines with a narrow passage, loss reduction can be effectively achieved by making the impeller inlet blade height larger than the nozzle vane height.

Next, we discuss the influence of thickening of the impeller blades and the nozzle vanes. **Figure 19** shows the results of prediction of overall turbine performance of Case 2, and a case where the impeller blade thickness has been increased to 1.5 times that in Case 2. The efficiency decrease resulting from thickening of the impeller blade tip is estimated to be approximately 0.4 points at the design pressure ratio. The change in characteristics of the mass flow rate is very small.

Figure 20 shows the results of prediction of overall turbine performance when thin or thick nozzle is installed. The efficiency does not appreciably change and the difference is 0.1 points or less. However, since the outlet angle of the thickened vane is smaller by 1 degree, the flow rate is correspondingly slightly larger (approximately 1%). **Figure 21** shows the distribution of the dissipation function around the vane's leading edge at the nozzle mean section. The dissipation function expresses the loss generation rate. Since the vane is
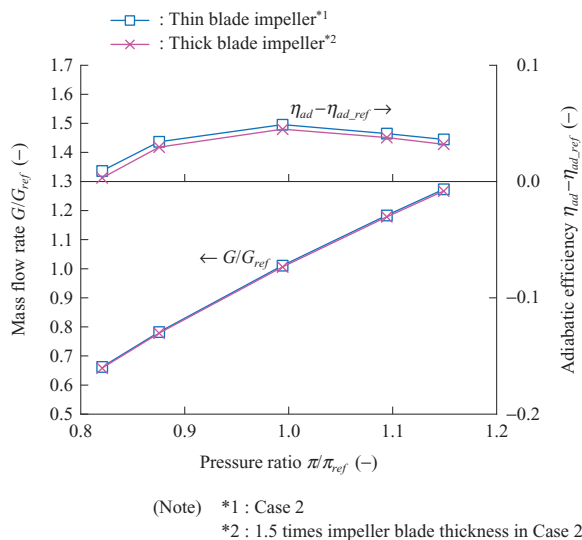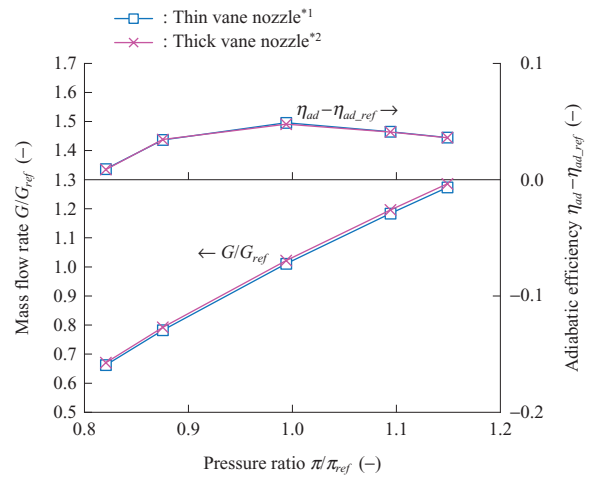

(Note) *1 : Case 2
        *2 : Thickening of leading edge of nozzle in Case 2

Fig. 20 Predicted overall turbine performance (influence of nozzle vane thickness)

cambered, a stagnation point exists on the pressure surface even though the inlet flow angle is 0 degrees. For the thin vane, no separation of the boundary layer is observed on either the suction surface or pressure surface, but for the vane with a blunt leading edge, a separation region is observed on the pressure surface. This separation region immediately reattaches on the downstream side, but losses occur in the separated shear layer. However, these losses are greatly exceeded by the total losses occurring in the ordinary attached boundary layer. Separation on the pressure surface of the leading edge due to the blunt leading edge of the nozzle is presumed to be unavoidable, but the accompanying performance degradation is very small.

4.4 Specifications and characteristics of compressor

Now we move onto the discussion on the compressor. **Table 3** lists the aerodynamic design specifications of the compressor for 10-kW unit. It is a two-stage centrifugal compressor, and the compressor impeller in each of the stages and one turbine impeller described in **Section 4.3** are on the same shaft. An intercooler is installed on the downstream side of the first-stage compressor and an aftercooler on the downstream side of the second-stage compressor, allowing
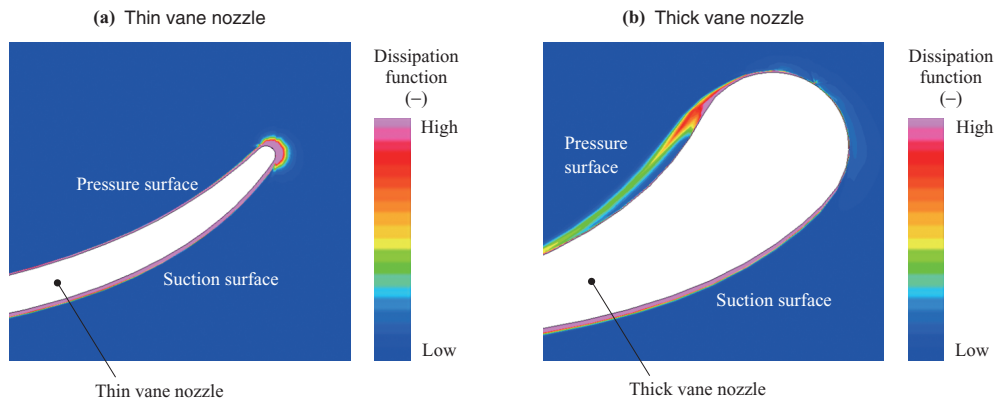

(Note) *1 : Case 2
        *2 : 1.5 times impeller blade thickness in Case 2

Fig. 19 Predicted overall turbine performance (influence of impeller blade thickness)

(a) Thin vane nozzle   **(b)** Thick vane nozzle

Fig. 21 Distribution of the dissipation function around the vane leading edge in the nozzle mean section

Table 3 Aerodynamic design specifications for the compressor (10-kW refrigerator)

Item	Unit	Value	
		First stage	Second stage
Type		Centrifugal	Centrifugal
Inlet temperature	K	303	303
Inlet pressure	kPa	500	710
Outlet pressure	kPa	730	1 030
Rotor speed	rpm	42 000	42 000
Mass flow rate	kg/s	0.960	0.960

the heat of compression generated by the compressor to be released outside the system. The specified pressure ratio is 2.0, which is not very high for a two-stage compressor, but, since the impeller speed is limited and the speed of sound in neon gas is higher than that in air, this specification corresponds to very high aerodynamic loading. Accordingly, in the development of this compressor, design was derived from an impeller type which — from amongst our impeller lineup for ordinary turbo-compressor products — is most highly loaded.

As illustrated in **Fig. 12**, the compressor, magnetic bearings, and motor, etc., are outside the cold box (in the normal-temperature area).

4.5 Influence of specific heat ratio

As described in **Section 4.4**, a highly-loaded high-efficiency impeller for ordinary turbo compressors is adopted in the design of this compressor. Such turbo compressors were developed for applications in which mainly air, oxygen, and nitrogen are compressed. These gases (diatomic molecules) and neon (monatomic molecules) have significantly different specific heat ratios (according to the kinetic theory of gases, that of the former is $\gamma = 7/5 = 1.4$, while that of the latter is $\gamma = 5/3 = 1.67$). Generally, even when actual operation conditions and test operation conditions have different gas properties and inlet states, compressor performance in actual operation can be predicted by adjusting the tip Mach number on the basis of the principle of similarity and appropriately correcting the difference in Reynolds number. The peripheral Mach number M_{u2} and Reynolds number Re are defined by the following equations.

$$M_{u2} = \frac{u_2}{c_{01}} \quad \cdots\cdots\cdots\cdots\cdots(15)$$

$$Re = \frac{u_2 b_2}{v_{01}} \quad \cdots\cdots\cdots\cdots\cdots(16)$$

Here, b_2 is the blade height at the impeller outlet, u_2 is the tip speed of the impeller, and c_{01} and v_{01} are respectively the speed of sound in the working fluid and its kinetic viscosity under inlet stagnation condition. However, when the specific heat ratio is different, the principle of similarity is not strictly applicable, and it is known that, as the specific heat ratio becomes larger, compressor efficiency decreases even when the tip Mach number and Reynolds number are unchanged[30], [31]. Hence, in this current development, the influence of the difference in specific heat ratio must be taken into account in addition to the influence of the differences in tip Mach number and Reynolds number that are based on differences in gas properties and inlet conditions.

We therefore performed a CFD analysis of the compressor using a fictitious working fluid. In this analysis, only the specific heat ratio was changed, with the peripheral Mach number and Reynolds number kept completely unaltered based on air under standard ambient conditions. **Figure 22** shows the results. In this figure, the design tip Mach number means the design value for air that was used when the original air compressor was developed, while the low tip Mach number is close to the specified value for the neon compressor and lower than the design tip Mach number. **Figure 22** shows that as the specific heat ratio increases, the efficiency and pressure coefficient decrease, and that the higher the tip Mach number, the more conspicuous this decrease becomes. However, at the tip Mach number level used for this design, the efficiency decrease due to the increase in specific heat ratio corresponding to the change from air conditions ($\gamma = 1.4$) to neon conditions ($\gamma = 1.67$) is 0.5 points or less, which is a relatively small value. It is accordingly not necessary to make any substantial shape modifications in consideration of neon conditions.

4.6 Results of compressor CFD analysis

Since the real gas effect for neon is negligible at normal temperature, the perfect gas approximation using ordinary gas properties can be applied to aerodynamic analysis of the

(a) Adiabatic efficiency change
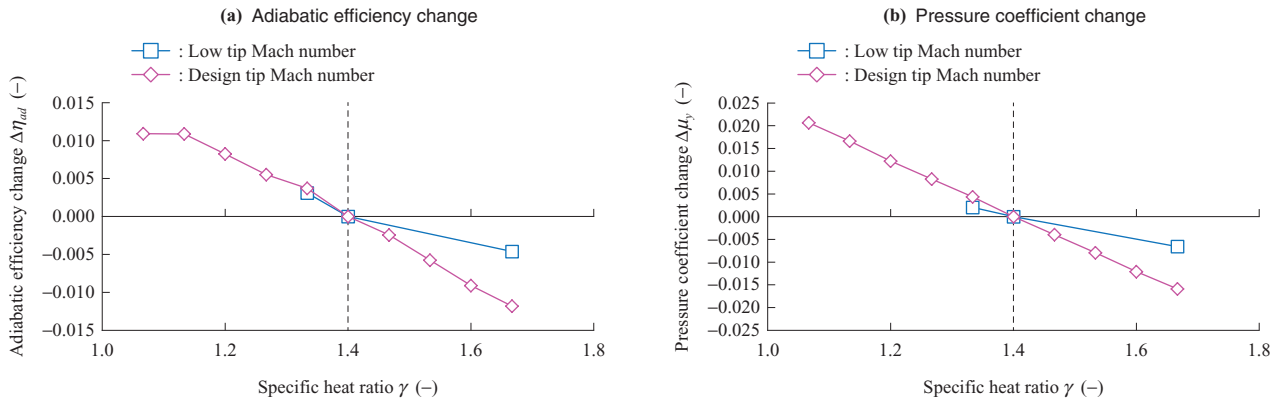
(b) Pressure coefficient change

Fig. 22   Influence of the specific heat ratio on the compressor performance

compressor. As in the case of the turbine analysis, a solver developed in-house was used as the CFD solver. The same approach as for the above-mentioned turbine analysis was applied to the finite difference scheme, turbulence model, and domain connection between rotor and stator, etc. The performance of the scroll was estimated not by applying a CFD model but by using a one-dimensional model.

Figure 23 shows the results of CFD analysis for prediction of overall performance of the first-stage and second-stage

compressors. The pressure ratio is slightly smaller than the target performance, and, in the actual compressor, a modification has been made to the compressor's shape in order to compensate for the pressure ratio deficiency, with an adjustment being made to the impeller tip diameter that satisfies the specified pressure ratio.

Figure 24 shows the relative Mach number distribution near the impeller shroud side around the design point. In both stages, the flow inside the impeller is smooth, and no
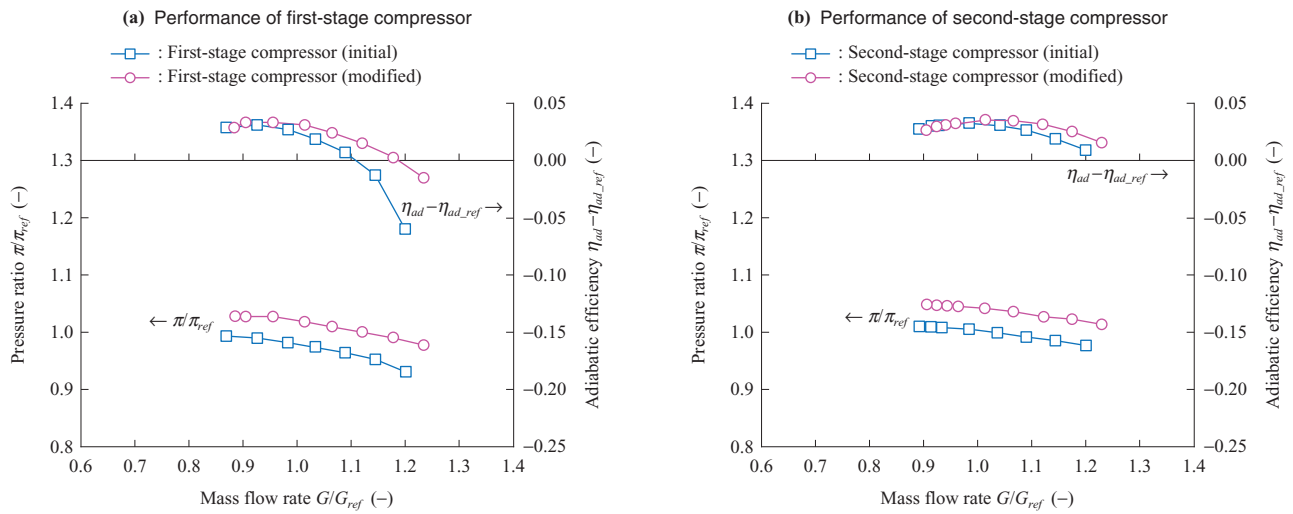

(a) Performance of first-stage compressor

(b) Performance of second-stage compressor

Fig. 23   Predicted overall compressor performance

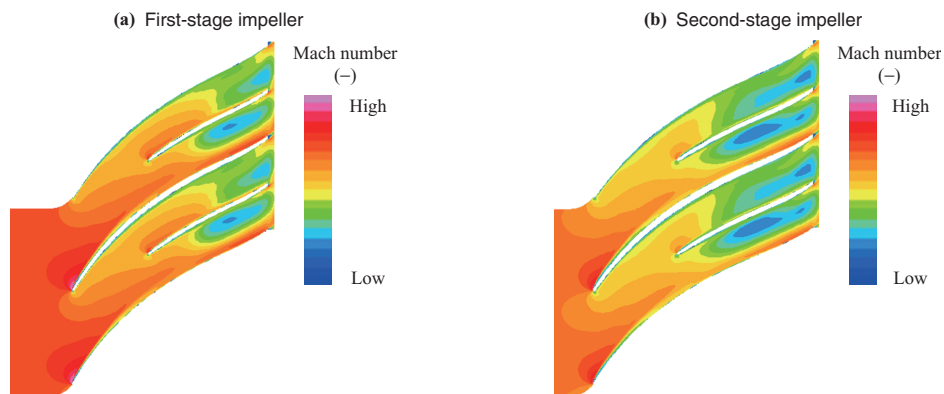**(a)** First-stage impeller

(b) Second-stage impeller

Fig. 24   Distribution of the relative Mach number in the impeller shroud section

problems occur such as separation or reverse flow, etc. Similarly, **Fig. 25** shows Mach number distribution at the diffuser mean section. The internal flow inside the diffuser is also favorable, and the flow field intended in the aerodynamic design is seen to be formed.

4.7 Summary of analyses of turbine and compressor for 10-kW unit

The above-described turbine and compressor have been incorporated into a 10-kW neon turbo-Brayton refrigerator system and put into actual operation. It has been confirmed that it delivers the favorable performance that was intended in the design. Some of the test results are also described in references (10) and (32).

5. Conclusion

This report has described the results of CFD analysis for the design and internal flow evaluation of a turbine and compressor for neon turbo-Brayton refrigerators. Since they operate under unusual conditions, their specifications and shapes are not necessarily aerodynamically ideal, but, through analysis and assessment using CFD, the accompanying losses and influences have been quantitatively evaluated, and the results can be used in design improvement.

This report summarizes evaluations based on CFD analysis that we have performed over the last 10 years regarding the aerodynamic design of turbines and compressors for neon turbo-Brayton refrigerators. Although neon refrigerators operate with an unusual fluid and under unusual operating conditions, we have demonstrated that CFD analysis, if theoretically customized in an appropriate manner, can be applied effectively to the aerodynamic design of such extraordinary machinery in a similar way to its application to ordinary machinery that use air, etc.

We will continue working toward the development of higher-performance, more highly-functional, and more reliable neon turbo-Brayton refrigerators by applying multiphysics analysis — and, in particular, heat transfer analysis and thermal stress analysis, etc. — to aerodynamic design.

REFERENCES

(1) New Energy and Industrial Technology Development Organization, Research Center for Strategic Technology : Toward a Technological-Strategy Planning of the Superconductivity Field, TSC Foresight, Vol. 4, 2015, pp. 1-18

(2) R. Radebaugh : Cryocoolers: the state of the art and recent developments, Journal of Physics: Condensed Matter, Vol. 21, No. 16, 2009, p. 164 219

(3) S. S. Kalsi : Cooling and Thermal Insulation Systems, Applications of High Temperature Superconductors to Electric Power Equipment, 2011, pp. 35-58

(4) Y. Bi : Cooling and Cryocoolers for HTS Power Applications, Applied Superconductivity and Electromagnetics, Vol. 4, No. 1, 2013, pp. 97-108

(5) S. Grohmann : Cooling technology for HTS power applications, ESAS Summer School, 2016

(6) New Energy and Industrial Technology Development Organization : Report of Research and Development of Fundamental Superconductivity-Application Technologies (Phase II) (FY2003-2007), 2008

(7) H. Hirai, M. Hirokawa, and A. Takaike : Development of a Neon Turbo-Expander with Active Magnetic Bearings, TAIYO NIPPON SANSO Technical Report, No. 28, 2009, pp. 1-5

(8) H. Hirai, M. Hirokawa, A. Takaike and S. Ozaki : Development of a Small Turbo-Compressor with Active Magnetic Bearings, TAIYO NIPPON SANSO Technical Report, No. 29, 2010, pp. 7-11

(9) New Energy and Industrial Technology Development Organization : Report of Technology Development Project of Yttrium-Series Superconducting Power Equipment (FY2008-2012), 2013

(10) S. Ozaki, H. Hirai, M. Hirokawa and S. Yoshida : Development of a 10 kW class neon turbo-Braytion refrigerator, TAIYO NIPPON SANSO Technical Report, No. 33, 2014, pp. 1-6

(11) S. Yoshida : Neon turbo-Brayton Refrigerator "NeoKelvin Turbo" for HTS Cable, International Workshop on Cooling-System for HTS Applications, 2015, pp. 1-20

(12) N. Nakamura, S. Komatsu, S. Ueda, M. Yoneda, M. Kudoh and A. Machida : Development of Cooling System and High-performance Refrigerator for HTS
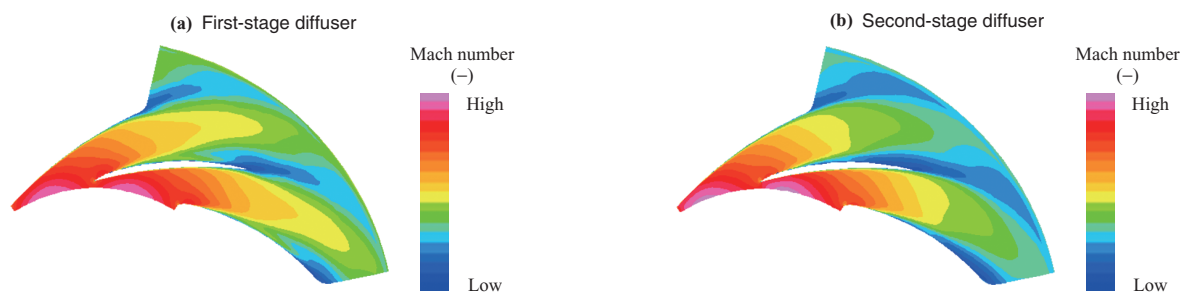
(a) First-stage diffuser

(b) Second-stage diffuser

Mach number (−)

High

Low

Fig. 25 Distribution of the Mach number in the diffuser mean section

Cable, Journal of Cryogenics and Superconductivity Society of Japan, Vol. 48, No. 7, 2013, pp. 382-387

(13) New Energy and Industrial Technology Development Organization : Report of Demonstrational Project of High-Temperature Superconducting Cable (FY2007-2013), 2014

(14) S. Bratt : Refrigerator Status – Performance DOE Peer Review Update, 2008

(15) A. Ravex : Refrigeration System Design, DOE Peer Review Update, 2010

(16) F. Schmidt, J. Maguire, T. Welsh and S. Bratt : Operation Experience and Further Development of a High-Temperature Superconducting Power Cable in the Long Island Power Authority Grid, Physics Procedia, Vol. 36, 2012, pp. 1 137-1 144

(17) H. M. Chang, C. W. Park, H. S. Yang, S. H. Sohn, J. H. Lim, S. R. Oh and S. D. Hwang : Thermodynamic Design of 10 kW Brayton Cryocooler for HTS Cable, Advances in Cryogenic Engineering AIP Conference Proceedings, Vol. 1 434, 2012, pp. 1 664-1 671

(18) C. H. Lee, D. M. Kim, H. S. Yang and S. Kim : Conceptual design of cryogenic turbo expander for 10 kW class reverse Brayton refrigerator, Progress in Superconductivity and Cryogenics, Vol. 17, No. 3, 2015, pp. 41-46

(19) J. Lee, C. Lee, H. Yang and S. Kim : Design of Thermodynamic Cycle and Cryogenic Turbo Expander for 2 kW Class Brayton Refrigerator, KEPCO Journal of Electric Power and Energy, Vol. 2, No. 2, 2016

(20) W. L. Swift : Turbo-Brayton Cryocoolers Spacecraft Thermal Control Handbook, Vol. 2 Cryogenics, The Aerospace Press, 2003, pp. 175-186

(21) R. W. Hill, J. K. Hilderbrand and M. V. Zagarola : An Advanced Compressor for Turbo-Brayton Cryocoolers, 16th International Cryocooler Conference, 2008, pp. 391-396

(22) M. Zagarola, J. McCormick and K. Cragin : Demonstration of an Ultra-Miniature Turboalternator for Space-Borne Turbo-Brayton Cryocooler, 17th International Cryocooler Conference, 2012, pp. 453-460

(23) J. Tanchon, J. Lacapere, A. Molyneaux, M. Harris, S. Hill, S. M. Abu-Sharkh and T. Tirolien : A Turbo-Brayton Cryocooler for Future European Observation Satellite Generation, 19th International Cryocooler Conference, 2016, pp. 437-446

(24) J. J. Breedlove, P. J. Magari and G. W. Miller : Cryocooler for Air Liquefaction onboard Large Aircraft, Advances in Cryogenic Engineering Transactions of the Cryogenic Engineering Conference, Vol. 53, 2008, pp. 838-845

(25) Y. Kaneko, S. Ohuchida, I. Morita and T. Kawakubo : Design Method of a Radial-Inflow Turbine for an Organic Rankine Cycle Generator using CFD with Perfect gas Assumption, 13th Asian International Conference on Fluid Machinery, 2016

(26) T. Kawakubo : Simple, stable and reliable modeling of gas properties of organic working fluids in aerodynamic designs of turbomachinery for ORC and VCC, 7th International Conference on Pumps and Fans, 2015

(27) T. Kawakubo and S. Ouchida : Perfect Gas Approximation of Organic Working Medium in Aerodynamic Design of ORC and VOC, 75th Turbomachinery Society of Japan (TSJ) Annual Plenary Meetings and Lecture Meetings, 2016

(28) R. H. Aungier : A fast, accurate real gas equation of state for fluid dynamic analysis applications, ASME Journal of Fluids Engineering, Vol. 117, 1995, pp. 277-281

(29) J. Kurokawa and T. Toyokura : Leakage Loss and Disc Friction Loss in Centrifugal Turbomachinery, Turbomachinery, Vol. 4, 1976, pp. 302-310

(30) V. F. Ris, Translated by I. Watanabe and M. Hamajima : Centrifugal Compressors, CORONA PUBLISHING, 1969, pp. 126-168

(31) S. K. Roberts and S. A. Sjolander : Effect of the Specific Heat Ratio on the Aerodynamic Performance of Turbomachinery, ASME Journal of Engineering for Gas Turbines and Power, Vol. 127, 2005, pp. 773-780

(32) S. Yoshinaga, K. Oda, H. Hirai and M. Hirokawa : Development of Turbine Compressors for Large-Capacity Turbo Refrigerators for Cooling High-Temperature Superconducting Power Equipment, Proceedings of the 78th Turbomachinery Society of Japan (TSJ) Lecture Meetings in Toyama, 2017